

# Comparison between Observation and Simulation of Sodium LGS Return Flux with a 20 W CW Laser on Tenerife

R. Holzlöhner<sup>\*a</sup>, D. Bonaccini Calia<sup>a</sup>, D. Bello<sup>b</sup>, D. Budker<sup>c</sup>, M. Centrone<sup>d</sup>, I. Guidolin<sup>a</sup>, W. Hackenberg<sup>a</sup>, S. Lewis<sup>a</sup>, G. Lombardi<sup>b</sup>, I. Montilla<sup>e</sup>, F. Pedichini<sup>d</sup>, F. Pedreros Bustos<sup>c</sup>, T. Pfrommer<sup>a</sup>, M. Reyes Garcia Talavera<sup>e</sup>, S. Rochester<sup>f</sup>

<sup>a</sup>European Southern Observatory (ESO), Garching, Germany; <sup>b</sup>Gran Telescopio de Canarias (GTC); <sup>c</sup>Johannes Gutenberg-Universität, Mainz, Germany, <sup>d</sup>INAF Rome, Italy, <sup>e</sup>Instituto de Astrofísica de Canarias (IAC); <sup>f</sup>Rochester Scientific LLC, El Cerrito, USA

## ABSTRACT

We report on the comparison between observations and simulations of a completed 12-month field observation campaign at Observatorio del Teide, Tenerife, using ESO's transportable 20 watt CW *Wendelstein* laser guide star system. This mission has provided sodium photon return flux measurements of unprecedented detail regarding variation of laser power, polarization and sodium D<sub>2b</sub> repumping. The Raman fiber laser and projector technology are very similar to that employed in the 4LGSF/AOF laser facility, recently installed and commissioned at the VLT in Paranal. The simulations are based on the open source *LGSBloch* density matrix simulation package and we find good overall agreement with experimental data.

**Keywords:** laser guide stars, sodium, Bloch simulations, numerical modeling

## 1. INTRODUCTION

Based on data obtained via an on-sky observing campaign [1] at the Observatorio del Teide on Tenerife (28.3°N), Spain with the ESO transportable *Wendelstein* laser guide star system [2], we present a comparison with our numerical return flux model. The experimental *Wendelstein* system is based on the same Raman fiber amplifier technology employed in the 4-Laser Guide Star Facility (4LGSF) on Unit Telescope 4 of ESO's Very Large Telescope (VLT) as part of the Adaptive Optics Facility (AOF) [3]. The laser system emits CW radiation at 589 nm with a linewidth of 1.35 MHz [4]. In this work, we compare return flux measurements with variable laser parameters (power, polarization, D<sub>2b</sub> repumping) and pointing directions on sky versus numerical simulations based on the *LGSBloch* package [5,6].

The campaign comprised five missions in June, September and December 2015, plus February and April 2016. The system was typically operated continuously for about one week each, observing the Laser Guide Star (LGS) with a 400 mm aperture telescope just a few meters away from the launcher.

### 1.1 Observation

The observing sequence and postprocessing pipeline were controlled by custom *IDL* scripts. Aperture photometry was performed using a Johnson V filter. See [1] in these proceedings for more details. An independently calibrated measurement of absolute sodium abundance has not been available.

Two different types of scans have been chiefly executed: launched laser power scans, and repumping power fraction scans. For the power scans, the launched laser power was increased in steps of a few watts. At each step, the laser polarization was cycled between linear and circular, plus switching D<sub>2b</sub> repumping on and off. For repumping scans, the D<sub>2b</sub> power fraction  $q$  was varied in steps from 0% (no repumping) to 26% at (near) constant laser power and polarization. We analyze these two types of scans in this work.

In further experiments, a toggling was performed between polarization states and repumping on/off at full laser power, accumulating statistical data across the sky, and moreover the laser linewidth was increased and the D<sub>2b</sub> frequency offset varied around 1.713 GHz.

\* email: rholzloe at eso.org; phone +49-89-3200-6671; www.eso.org

## 2. RESULTS

### 2.1 Power Scans

In order to cover a variety of experimental conditions, we have studied laser power scans. In these scans, the laser power was raised from zero in increments of a few watts, measuring the LGS return flux in each step. The dots in Fig. 1 show the measured flux on the ground in units of  $10^6$  photons/s/m<sup>2</sup> as a function of launched laser power in  $D_{2a}$  and  $D_{2b}$  (*i.e.*, ignoring the “red” sideband that most modulators also generate). The four colors denote linear polarization (red:  $q = 0$ , pink:  $q > 0$ ) vs. circular polarization (blue:  $q = 0$ , green:  $q > 0$ ), where  $q$  is the repumping power ratio defined as

$$q = \frac{P_{D_{2b}}}{P_{D_{2a}} + P_{D_{2b}}}, \quad (1)$$

and  $P_{D_{2a}}$  and  $P_{D_{2b}}$  represent the power resonant with the  $D_{2a}$  and  $D_{2b}$  lines, respectively. At each power setting in the scan, the polarization state and  $q$  were changed, collecting measurements of four different states, each with 10 s exposure time. In the same frame as the LGS, a photometric natural star was observed within 60 arcsec of the LGS, and the measured LGS return flux is corrected for atmospheric transmission variations obtained from fluctuations in the natural star’s brightness. The measurements have been taken in various pointing directions, shown as ALT (elevation angle) and AZ (azimuth) in the lower right-hand corner of Fig. 1 (North: AZ = 0°, East: AZ = 90°).

The simulation includes the freely available package *LGSBloch* [6], written in *Mathematica*. This code uses density matrices (Bloch equations) to solve the quantum mechanical problem of determining the steady-state hyperfine sodium atom populations within an ensemble of 100–200 Doppler velocity classes found in the mesosphere [5]. The physical

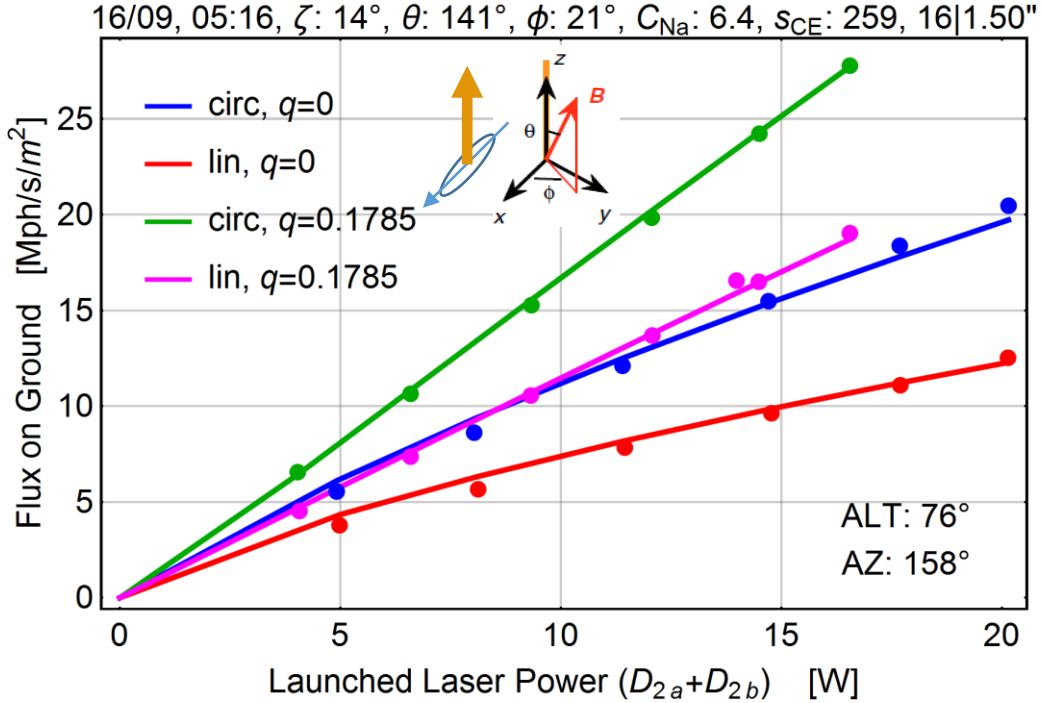


Figure 1. Measured return flux vs. launched laser power of four power scans (dots) in comparison with simulations (curves). The colors distinguish the launched polarization state and the  $D_{2b}$  repumping power fraction  $q$ . The plot headline yields the observing date, time and laser angles  $\theta$  and  $\phi$  to the magnetic field, as well as the applied simulation best fit parameters. Inset: laser beam coordinate system with beam along  $z$  and polarization ellipse along  $x$ , plus the geomagnetic field vector  $B$ .

target of the simulation is thus “microscopic” sodium excitation within only a small parcel of air in the mesosphere, or, alternatively, in a sodium vapor cell [4]. All simulations discussed by Holzlöhner *et al.* in [5] fit this description (see Fig. 3 in this reference for typical plots of sodium return flux versus irradiance).

Building upon this microscopic simulation, the task is now to compute the macroscopic LGS return flux by integrating over the entire column irradiated by the laser in the sodium layer, as described in detail in [7]. To do so, we use a three-step approach. In the first step, we calculate a data cube of the return flux, where the cube dimensions are laser irradiance in the sodium layer, altitude above sea level, and the polar angles  $\theta$  and  $\phi$  of the geomagnetic  $B$ -field. These angles are defined in a Cartesian coordinate system where the laser beam propagates along  $z$  and the major axis of the polarization ellipse is oriented parallel to the  $x$ -axis, as depicted in the inset of Fig. 1 (polarization ellipse shown in blue). We apply gas density and temperature profiles from the MSIS-E-90 atmospheric model [8]. On the other hand, laser polarization, linewidth and magnitude of the  $B$ -field are kept constant within each data cube.

In the second step, a numerical integration is carried out for each experimental pointing direction on sky, running along the laser beam in the sodium layer and using a histogram of laser irradiance obtained from Monte Carlo physical optics simulations [9]. The latter takes into account wavefront errors in the launched beam measured in the laboratory, a standard multi-layer turbulence profile. We have used a set of seven irradiance histograms corresponding to DIMM seeing values of 0.5”, 0.75”, ..., 3.0” (defined at 500 nm and pointing at zenith). The actual zenith angle and azimuth of each observation are taken into account in the above. In the integration, we also use the same set of five different sodium density profiles from lidar observation at the LZT in Vancouver, Canada of 2008 as in [7].

In the third step, the return flux resulting from each of the  $5 \times 10 = 50$  different combinations of environmental conditions are least-squares fitted to the four power scans in each pointing direction (the blue, red, green and pink dots in Fig. 1). Applying the same fit parameters to all four power scans in a set is justified by the fact that they have been observed interlaced with each other, leaving little time for the mesospheric conditions to vary. This procedure yields 50 averaged squared fitting errors; of which we select the lowest (“best fit”). The headline of the plot in Fig. 1 shows the date and UTC time of the observation, zenith angle  $\zeta$  (where  $\zeta = 90^\circ - \text{ALT}$ ), magnetic field zenith angle  $\theta$  and azimuth  $\phi$ , followed by the best fit parameter  $C_{\text{Na}}$  and the LGS coupling efficiency  $s_{\text{CE}}$ . Finally, there is a string like 16|1.50”, where 16 denotes the best fit sodium profile (this particular profile was recorded on July 16, 2008 at LZT, see Fig. 3 in [7]) and 1.50” denotes the seeing corresponding to the best fit irradiance histogram. We believe that our data reduction method can validate the model and infer  $C_{\text{Na}}$  at the same time, even in the absence of an external independently calibrated measurement of the sodium abundance.

The quantity  $s_{\text{CE}}$  in units of photons/sr/s/W/(atoms/m<sup>2</sup>) is a figure of merit meant to allow efficiency comparisons between different sodium LGS systems [5]

$$s_{\text{CE}} = \frac{\Phi H^2 X}{P T_a^{2X} C_{\text{Na}}}, \quad (2)$$

where  $\Phi$  denotes the return flux on the ground,  $H$  is the vertical altitude of the sodium centroid above the telescope,  $X = \sec(\zeta)$  is the airmass,  $P$  is the launched laser power and  $T_a$  is the one-way atmospheric transmission at 589 nm at zenith (the latter is raised to the power  $2X$  to account for the double pass transmission along the slanted line of sight).

Since there is no simple obvious way of accounting for the return flux dependence on  $\theta$  and the zenith angle  $\zeta$  (observations at higher airmass imply larger lateral beam extent in the mesosphere, causing a reduction in irradiance and thus in optical pumping), the values of  $s_{\text{CE}}$  depend on the laser pointing. When comparing different LGS systems using  $s_{\text{CE}}$ , it is thus important to do so at similar angles  $\theta$  and  $\zeta$ . In particular, when pointing the laser near the geomagnetic “hotspot” on sky (Tenerife: ALT = 36.9°, AZ = 174.4° (*i.e.*, slightly East of South)), it is possible to obtain peak values of  $s_{\text{CE}}$  which, however, have little practical relevance for good sky coverage in telescopes with sodium LGS adaptive optics.

Figures 2–6 show fitted power scan observations of the five different missions to Mt. Teide. Overall, the curves agree well with the dots, albeit with some notable exceptions as in several of the April 2016 mission plots. December 2015 had only two powerscan sets. In some cases in February and April 2016, the best fit seeing is 3.0” which is the largest seeing value that we ran physical optics simulations for, hence it may be that the best fit seeing is yet larger.

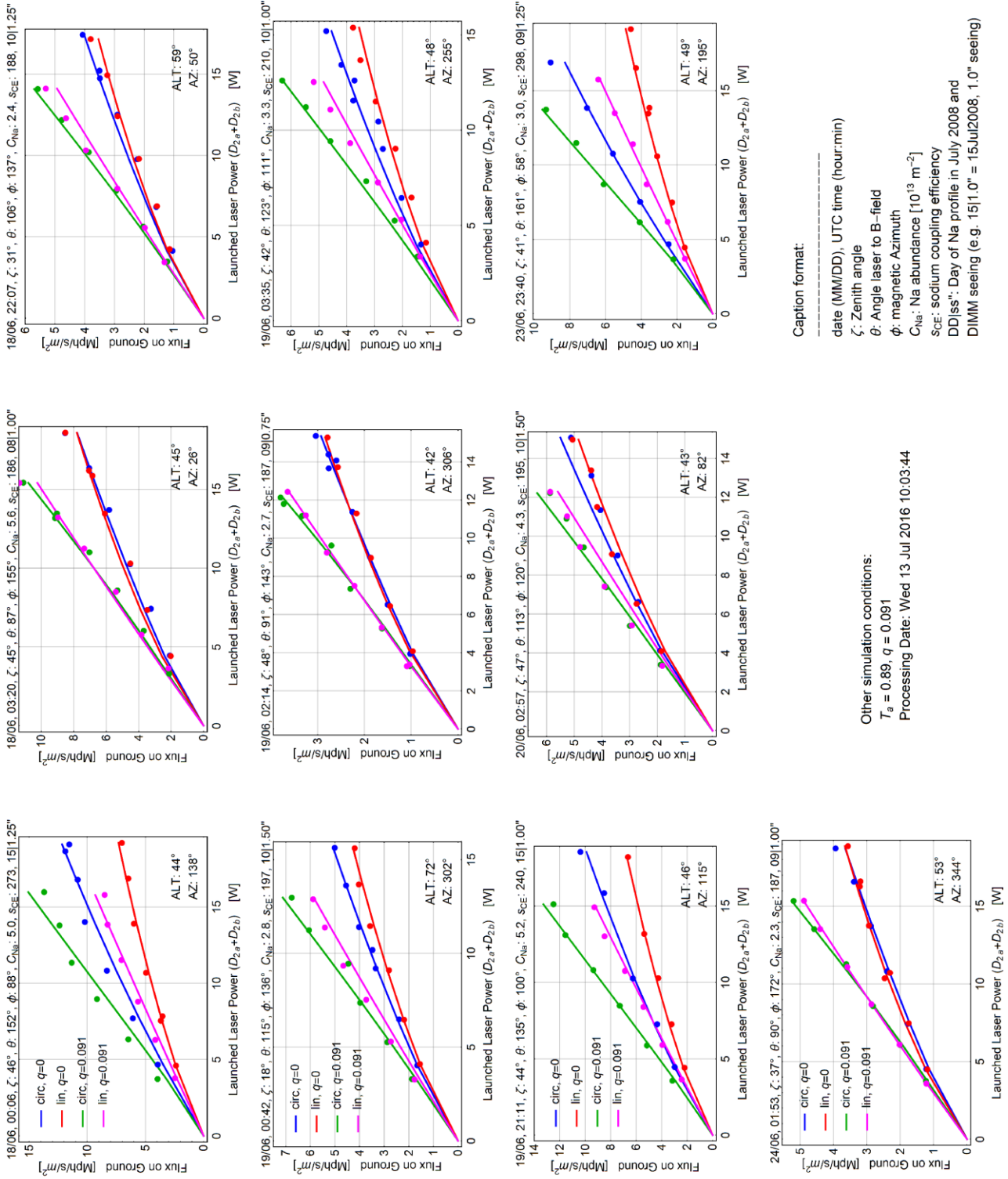


Figure 2. Power scan fits of the mission in June 2015

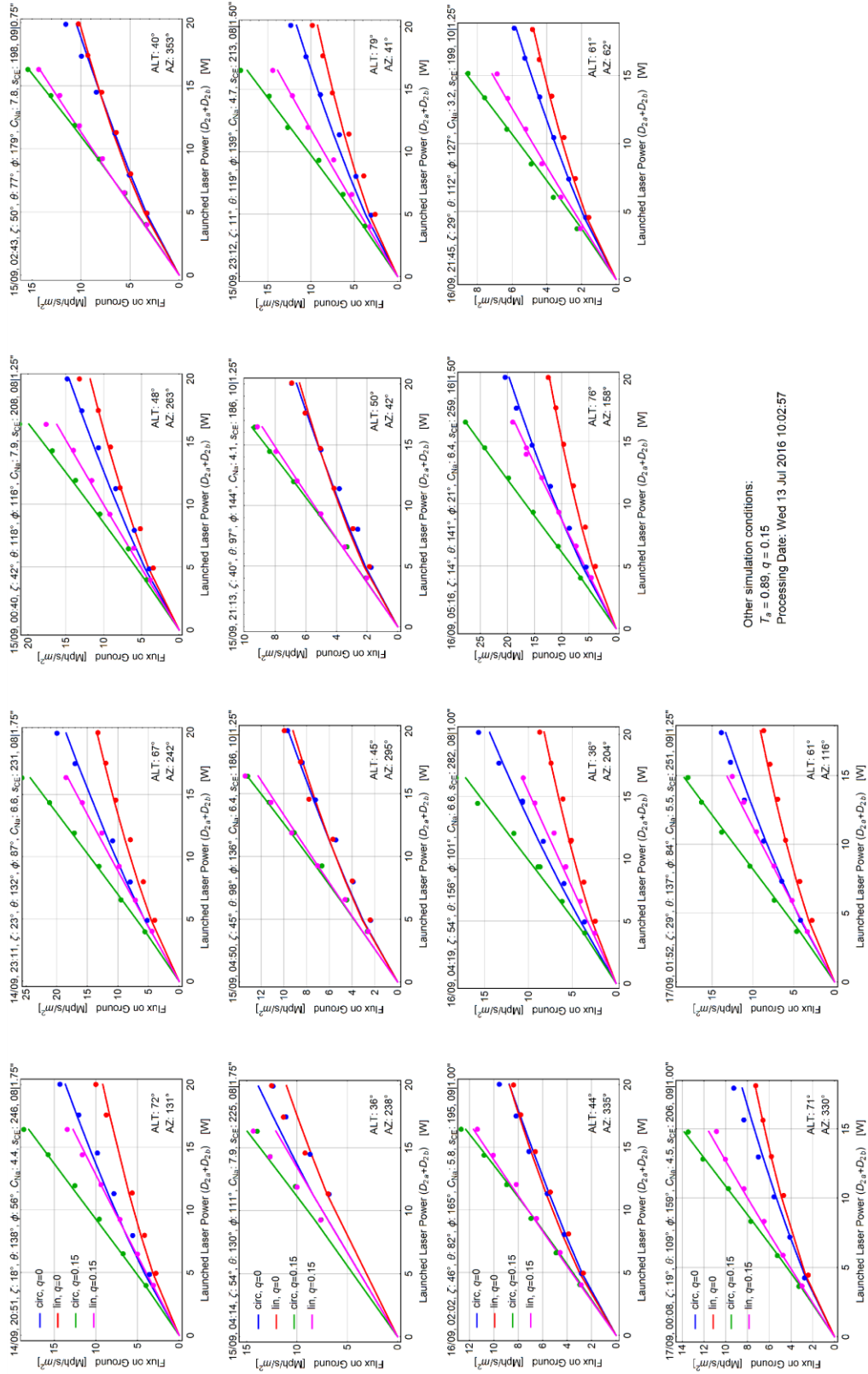


Figure 3. Power scan fits of the mission in September 2015

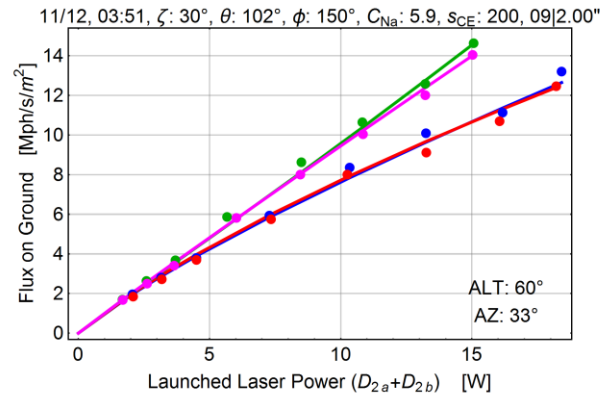
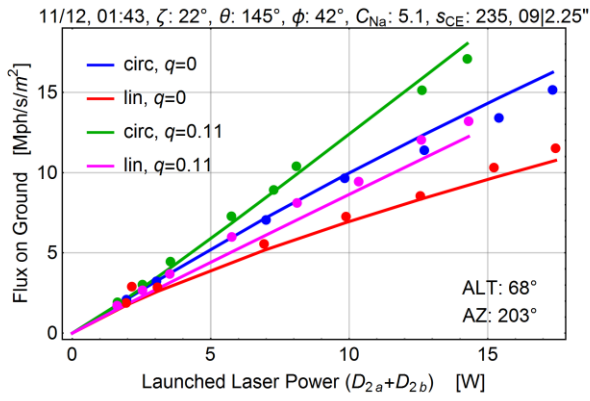


Figure 4. Power scan fits of the mission in December 2015

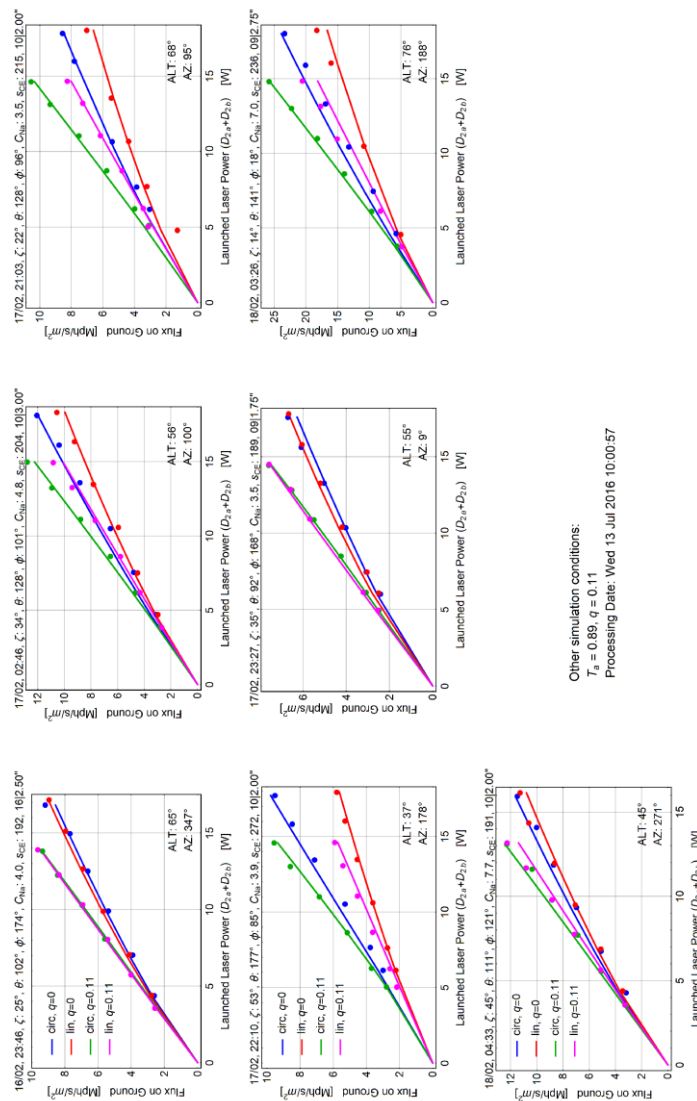


Figure 5. Power scan fits of the mission in February 2016

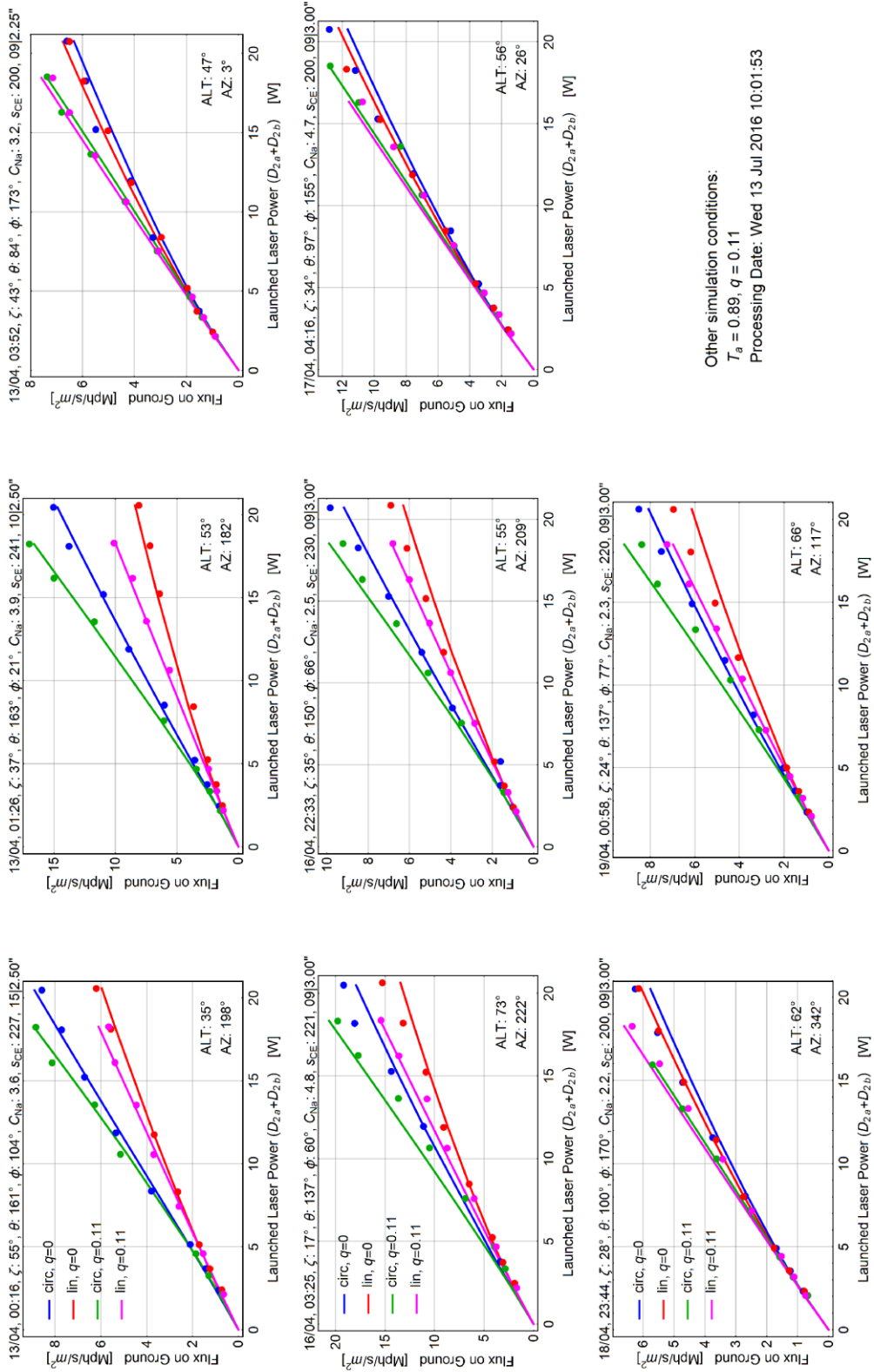


Figure 6. Power scan fits of the mission in April 2016

The winter/spring season 2015/2016 was an exceptionally hard one on the Canary Islands with low temperatures, record snowstorms and high winds, and it cannot be ruled out that the seeing has exceeded 3.0'' at times. Moreover, windshake of the receiver telescope (which has no dome) can blur the images, which may have limited the accuracy of the photometry. If the spot size in the mesosphere grows, the laser irradiance in the sodium layer is reduced, which tends to diminish the return flux differences among the four different laser polarization/repumping states due to less efficient optical pumping, compatible with the observations e.g. on 18/02/16, 16/04/16 and 19/04/16.

The two top plots in the center column of Fig. 2, and the plot on the left bottom indicate that when pointing about perpendicular to the  $B$ -field ( $\theta \sim 90^\circ$ ), the difference between linear and circular polarization becomes small. However, the repumping still yields a boost, a finding reflected in the similarity of the blue curve in Fig. 3a to that in Fig. 3b of [6] with  $\theta = 90^\circ$ ,  $q = 0.12$  and analogously the pink curve in Fig. 3a to that in Fig. 3b with  $\theta = 90^\circ$ ,  $q = 0$  in the same reference. Conversely, once  $\theta$  shifts away from  $90^\circ$ , as for instance in the lower right plot of Fig. 2 ( $\theta = 161^\circ$ ), the four curves spread apart. When approaching the magnetic "hotspot" as in the plot in row 2, column 2 of Fig. 5 ( $\theta = 177^\circ$ ), the blue and green curves, as well as the red and pink curves, close their gaps, indicating that polarization trumps repumping in this limit. This behavior is supported by the red and green curves in Fig. 3a,b of [6], albeit only up to irradiances of about 1 W/m<sup>2</sup>. Near the hotspot, the fit value of  $s_{CE}$  can approach and even exceed 300 photons/sr/s/W/(atoms/m<sup>2</sup>).

We always find that the green dots and curve (circular,  $q > 0$ ) show the highest and the red dots and curve (linear,  $q = 0$ ) the lowest return. While the red curve gently bends downwards due to a complicated interplay of saturation effects, the green curve is flat or even bends slightly upwards, indicating optical pumping. Because of the generation of the unwanted red sideband (a mirror image of the  $D_{2b}$  sideband), the green and pink curves stop a few watts before the blue and red curves.

## 2.2 Repumping power fraction scans

Another type of scan that has been carried out at Observatorio del Teide consisted of varying the fraction  $q$  of the  $D_{2b}$  repumping from 0 to 26%, while keeping the total *emitted* laser power  $P_{tot} = P_{D_{2a}} + 2 P_{D_{2b}}$  constant (consequently, the *useful* launched laser power  $P_{D_{2a}} + P_{D_{2b}}$  falls off with growing  $q$ ). Figure 7 shows two scans recorded on 16/09/2016 within 15 minutes with circular (left) and linear (right) polarization, respectively, following the same natural reference star. As previously, the dots denote the observation and the curves represent the simulation. The data fitting procedure was very similar to that used for the power scans of the previous subsection. We chose here to express the results in terms of  $s_{CE}$  because of the variable useful laser power and in order to facilitate comparisons among different pointing directions at different airmasses.

It is interesting to note that the best fit values for  $C_{Na}$  hardly differ and the best fit sodium profile is the same in the plots of Fig. 7, an indication that the simulation yields the correct return flux ratio when comparing circular with linear polarization over  $0 \leq q \leq 0.26$  (the best fit seeing, however, does differ between 1.25'' and 1.75''). The data point at  $q = 0$  has been excluded from the fits as they do not seem to match the curve. We are investigating, among other possible causes, whether repumping was indeed completely turned off at this data point. The experiment vs. simulation agreement in the two examples looks (very) good, however when surveying all available repumping power fraction scans in Fig. 8–12, it becomes obvious that this is not always the case, in particular not for the last three missions in December 2015, February and April 2016 when the seeing was poor. In some of the plots with bad agreement, the dots scatter so that it seems possible that there may have been strong windshake, as discussed in the previous subsection. In several cases, the dots begin to fall off rapidly after about  $q = 10\%$ ; in other cases, the observed flux hardly varies at all with  $q$ .

In the plots with good fitting agreement and with circular polarization, the maximum return flux is achieved near  $q = 15\%$  and lies about 4% higher than at  $q = 10\%$ , the repumping power fraction specified in the 4LGSF lasers.

Further, it is worth pointing out how slowly the simulation curves of LGS efficiency drop off with  $q$ . If the laser light is generated by a Raman fiber amplifier, as is the case with the *Wendelstein* system and the 4LGSF lasers manufactured by Toptica/MPBC [10], the achievable power is limited by stimulated Brillouin scattering (SBS) in the infrared. Since the SBS lines at  $D_{2a}$  and  $D_{2b}$  do not influence each other thanks to their large frequency separation of 1.71 GHz, one could thus propose to increase the useful laser power by raising  $q$  to 30% or more ( $q = 50\%$  would mean equal powers in  $D_{2a}$  and  $D_{2b}$ ) without exceeding the SBS threshold. Moreover, it is in principle possible to suppress the unwanted red sideband using single-side modulation schemes, thereby reducing the amount of wasted laser light and light pollution from uplink beam scattering. It should thus be possible to build a 30 W laser with the existing amplifier technology.

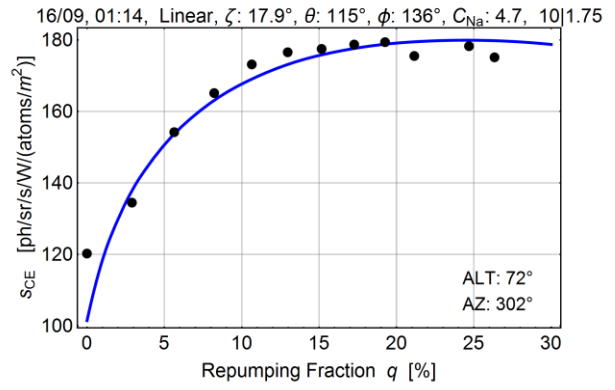
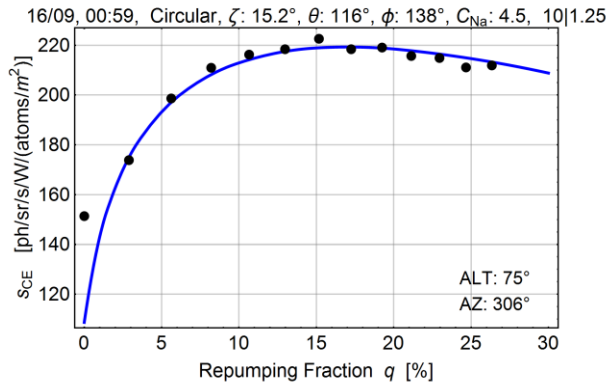


Figure 7. Two  $D_{2b}$  repumping power fraction scans recorded on 16/09/2015 within 15 minutes, tracking the same star (dots: measurements, curves: best fit simulation). Left: circular, right: linear polarization.

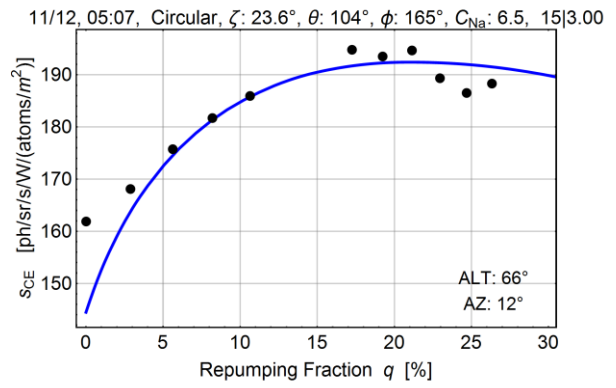
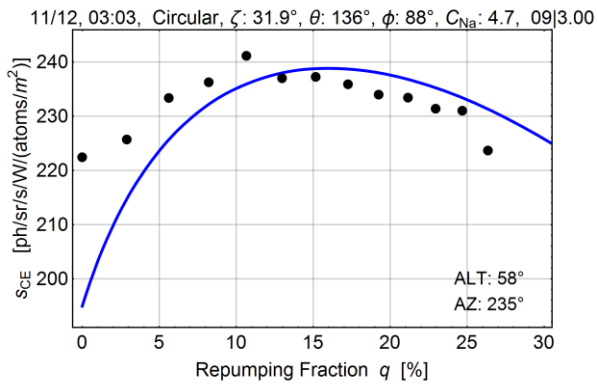


Figure 8. Repumping power fraction scan fits of the mission in December 2015 with poor seeing

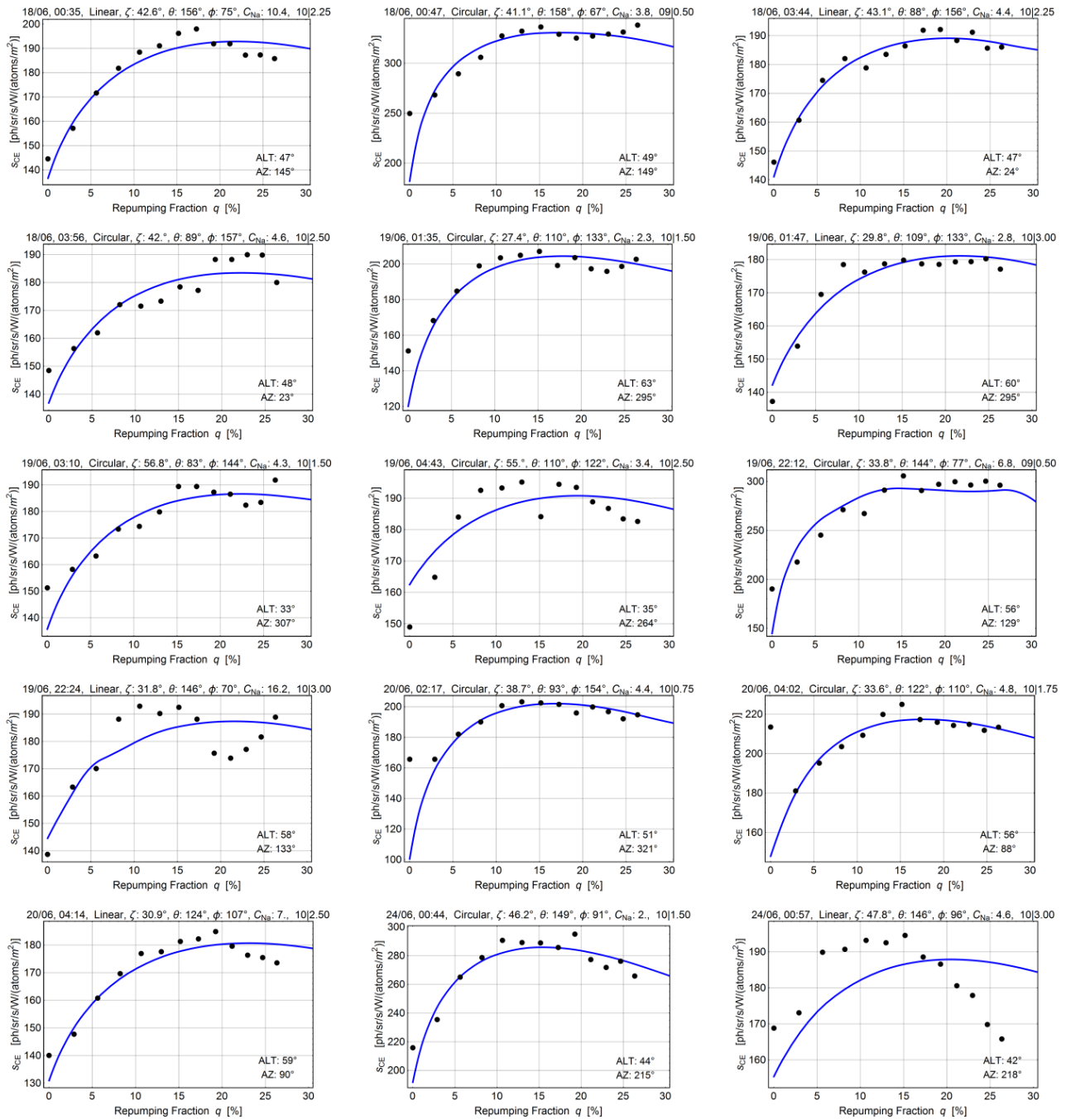


Figure 9. Repumping power fraction scan fits of the mission in June 2015

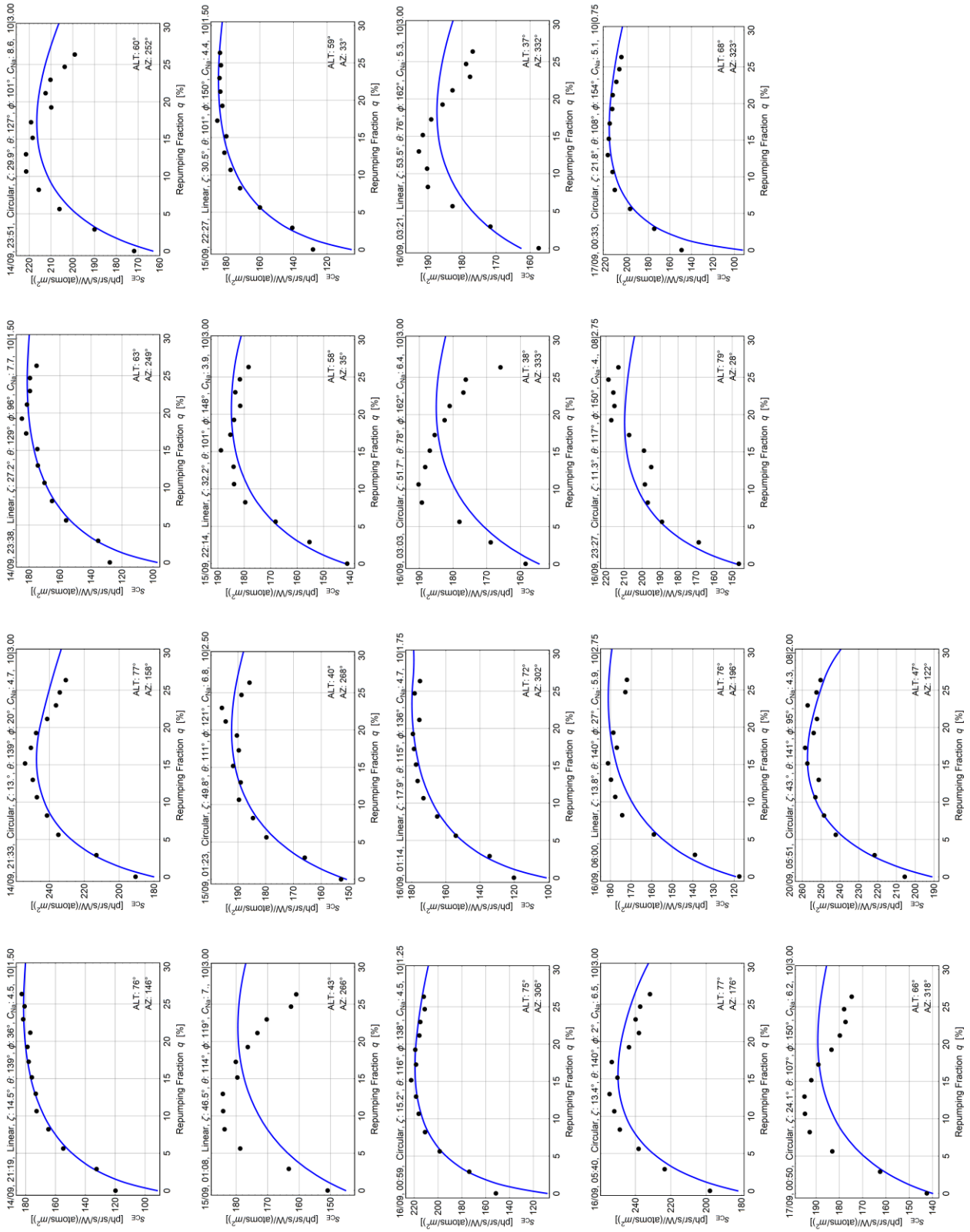


Figure 10. Repumping power fraction scan fits of the mission in September 2015

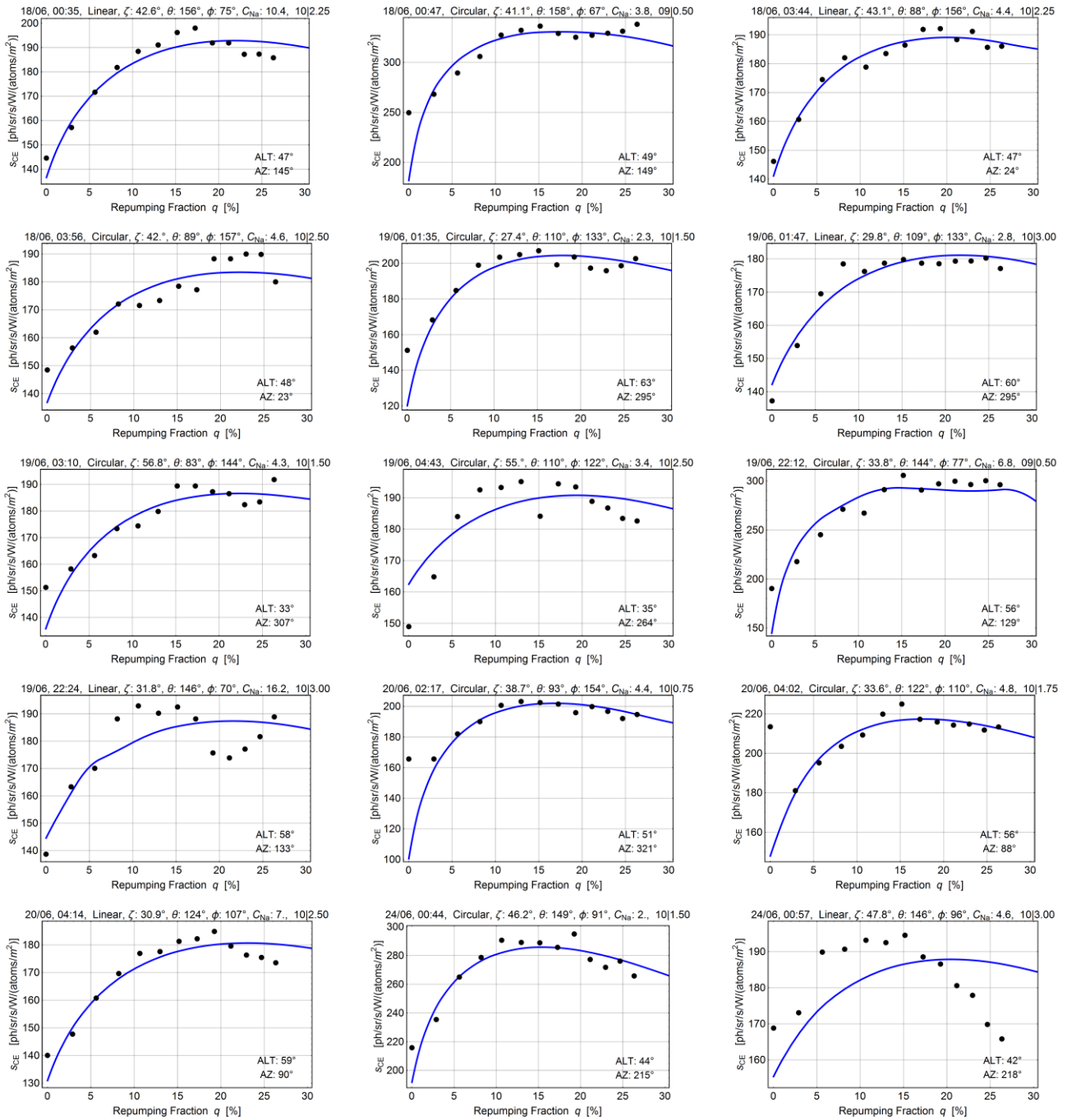


Figure 11. Repumping power fraction scan fits of the mission in February 2016

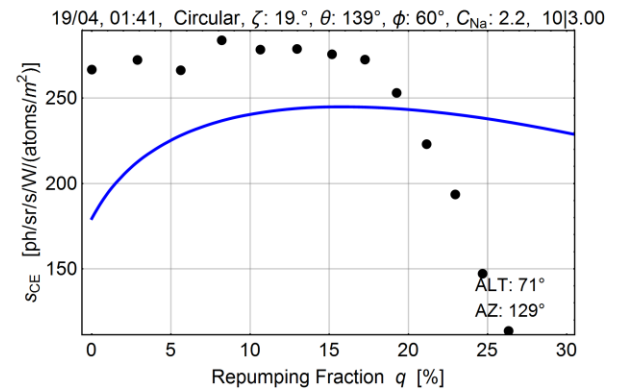
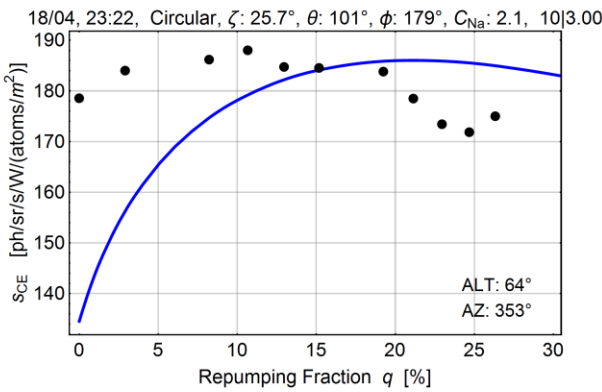
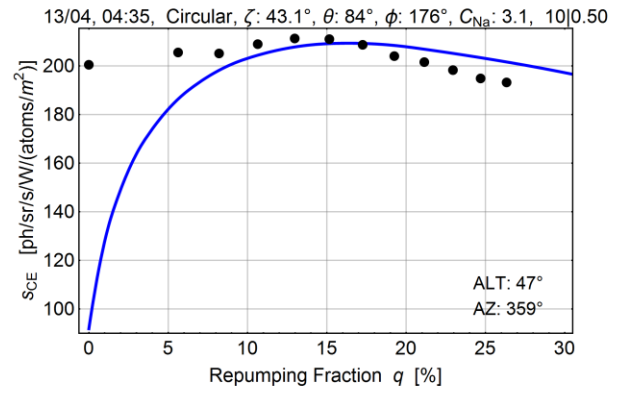
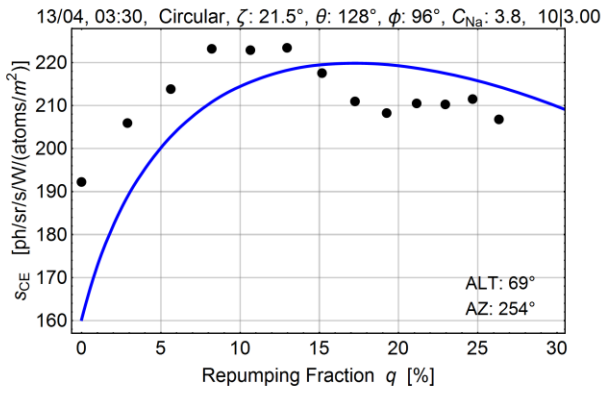
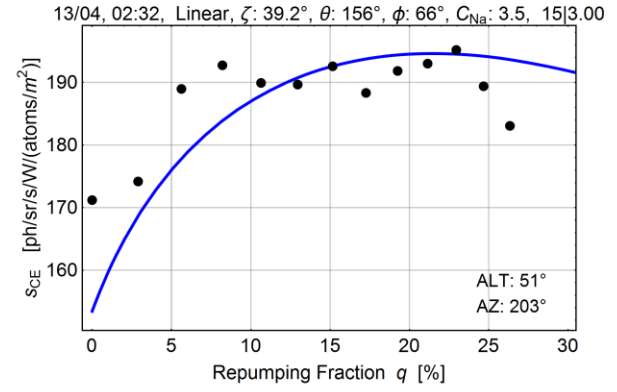
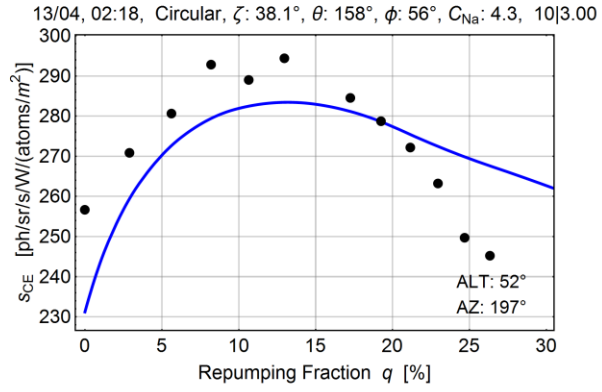
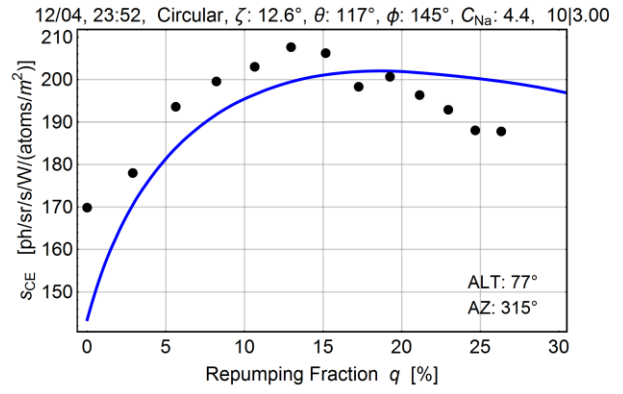
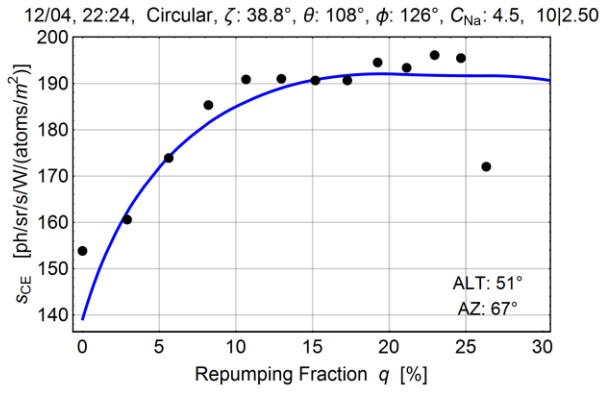


Figure 12. Repumping power fraction scan fits of the mission in April 2016

### 2.3 Correlations and sodium abundance time series

In this subsection, we address the question whether the best fit values of  $C_{Na}$  are correlated with the laser pointing. Any such systematic correlation would indicate a flaw in the numerical model, since  $C_{Na}$  is obviously a purely geophysical quantity and the laser pointing directions were picked in no particular order.

The upper left subplot in Fig. 13 shows  $C_{Na}$  in blue as a function of time for the June 2015 mission (the solid gray vertical lines denote midnight UTC = local (summer) time on the Canaries). The red dots indicate the corresponding laser zenith angles  $\zeta$ , scaled by 0.1. In particular, near the second solid gray vertical line, it is evident that despite large variations in  $\zeta$ , the best fit  $C_{Na}$  remains almost constant. The other plots show  $C_{Na}$  versus  $\zeta$  and the magnetic angles  $\theta$  and  $\phi$ . Figures 14–16 show the same for the September 2015, February and April 2016 missions (we do not analyze the December 2015 mission since it only has two data points).

Considering all plots in Figs. 13–16, we find no systematic correlations. The fit value of  $C_{Na}$  can vary by a factor of 2 within one night (e.g., the first night in the September 2015 mission or the last night in February 2016), although most nocturnal variations are smaller.

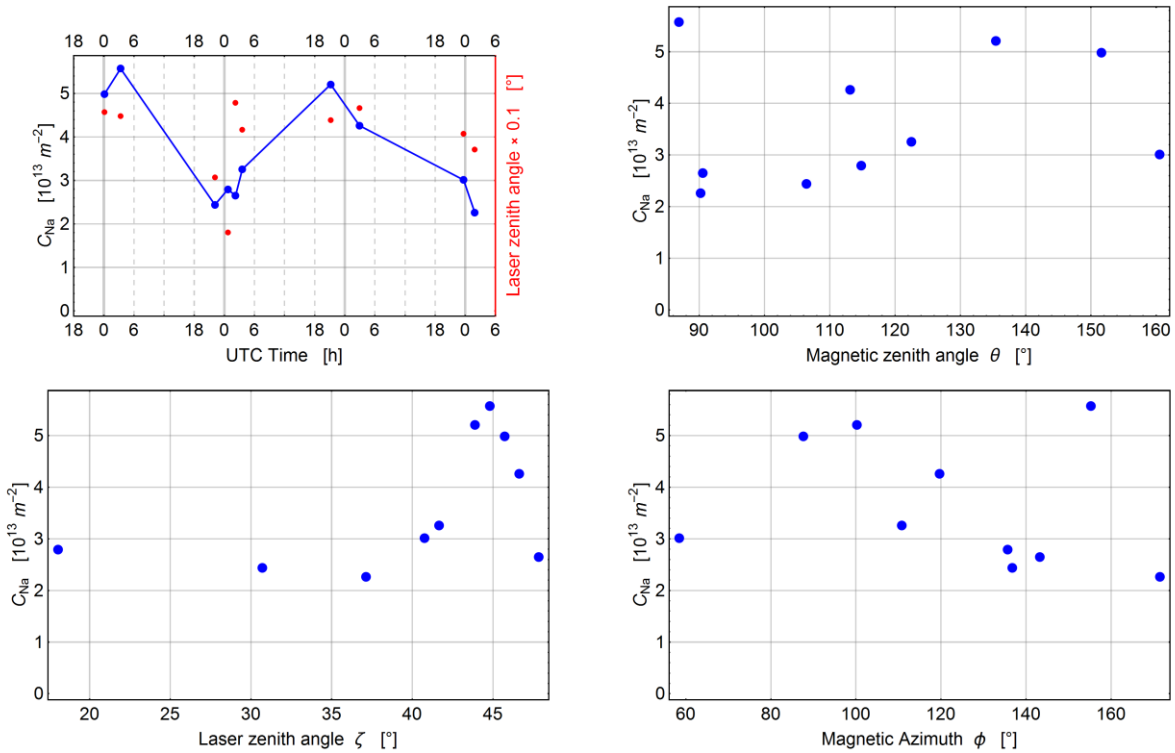


Figure 13.  $C_{Na}$  trend and correlations with laser pointing for June 2015 mission. Upper left panel, then counter-clockwise:  $C_{Na}$  and  $\zeta$  vs. time;  $C_{Na}$  vs. laser zenith angle  $\zeta$ ;  $C_{Na}$  vs. magnetic zenith angle  $\theta$ ;  $C_{Na}$  vs. magnetic azimuth  $\phi$

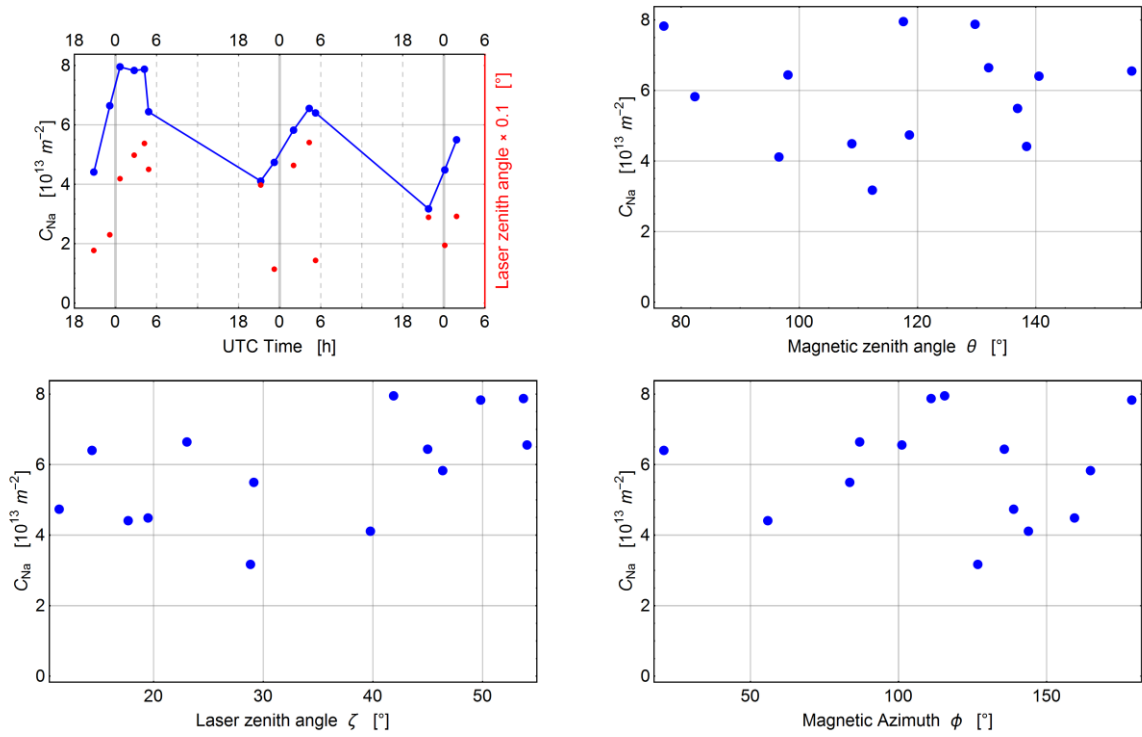


Figure 14.  $C_{Na}$  trend and correlations with laser pointing for September 2015 mission. Upper left panel, then counter-clockwise:  $C_{Na}$  and  $\zeta$  vs. time;  $C_{Na}$  vs. laser zenith angle  $\zeta$ ;  $C_{Na}$  vs. magnetic zenith angle  $\theta$ ;  $C_{Na}$  vs. magnetic azimuth  $\phi$

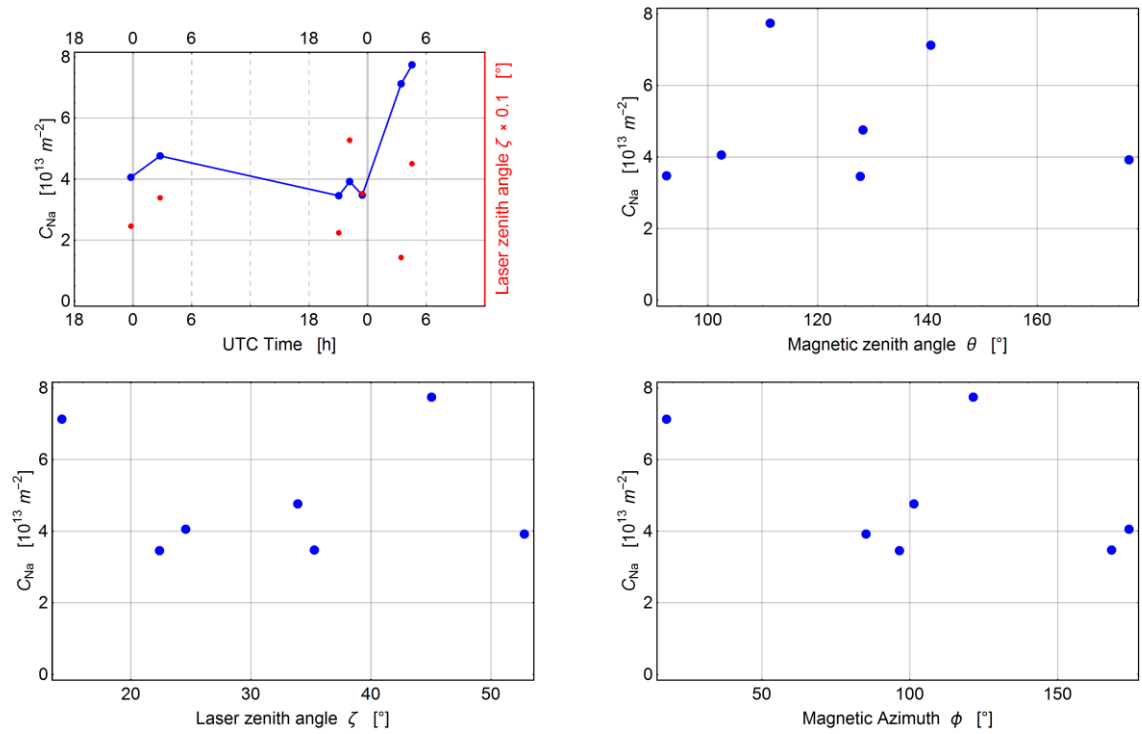


Figure 15.  $C_{Na}$  trend and correlations with laser pointing for February 2016 mission. Upper left panel, then counter-clockwise:  $C_{Na}$  and  $\zeta$  vs. time;  $C_{Na}$  vs. laser zenith angle  $\zeta$ ;  $C_{Na}$  vs. magnetic zenith angle  $\theta$ ;  $C_{Na}$  vs. magnetic azimuth  $\phi$

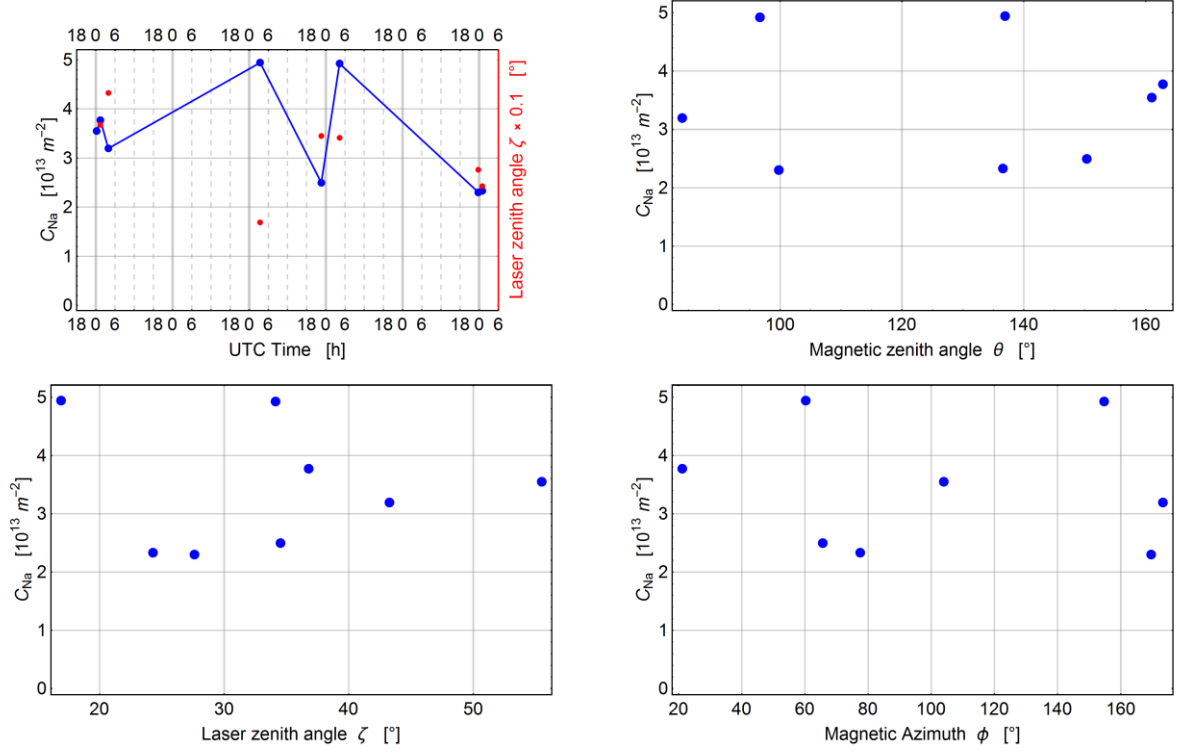


Figure 16.  $C_{Na}$  trend and correlations with laser pointing for April 2016 mission. Upper left panel, then counter-clockwise:  $C_{Na}$  and  $\zeta$  vs. time;  $C_{Na}$  vs. laser zenith angle  $\zeta$ ;  $C_{Na}$  vs. magnetic zenith angle  $\theta$ ;  $C_{Na}$  vs. magnetic azimuth  $\phi$

## 2.4 Seasonal sodium abundance

Finally, we list the median  $C_{Na}$  with standard deviations  $\sigma$  of the five observing missions in Table 1. The total median of all missions is  $C_{Na} = 4.1 \times 10^{13}$  atoms/m<sup>2</sup>. In Fig. 18, the red dots show the median  $C_{Na}$  and the red bars extend to  $\pm\sigma$  (again, note that the December 2015 mission only comprised two data points). The blue curve is a fit function to GOMOS satellite data by Fussen *et al.* [11] (see Eq.(8), with a fit uncertainty of  $0.81 \times 10^{13}$  atoms/m<sup>2</sup>), evaluated at the Teide latitude  $28.3^\circ\text{N}$ . The sodium abundance varies annually and the variations grow with the geographic latitude. In the northern hemisphere,  $C_{Na}$  tends to dip around May and peak around November. In addition, there are annually recurring meteor showers like the Perseids in mid-August, the Southern Taurids (10 Sep–20Nov) or the Leonids in mid-November that could generate temporary spikes in  $C_{Na}$ .

Table 1: Median  $C_{Na}$  and standard deviations  $\sigma$  of the five observing missions

Mission	$C_{Na}$ [ $10^{13}$ atoms/m <sup>2</sup> ]	$\sigma$ [ $10^{13}$ atoms/m <sup>2</sup> ]
June 2015	3.1	1.2
September 2015	6.1	1.5
December 2015	5.5	0.6
February 2016	4.1	1.8
April 2016	3.4	1.1

We also compare against two lidar measurements from the literature from Ge *et al.* [12] and Roberts *et al.* [13]. In all three comparisons so far, the September 2015 median abundance of  $C_{Na} = 6.1 \times 10^{13}$  atoms/m<sup>2</sup> seems high, however, the error bars in Fig. 7 of Ref. [11] for September of both GOMOS and OSIRIS satellite data do include this value.

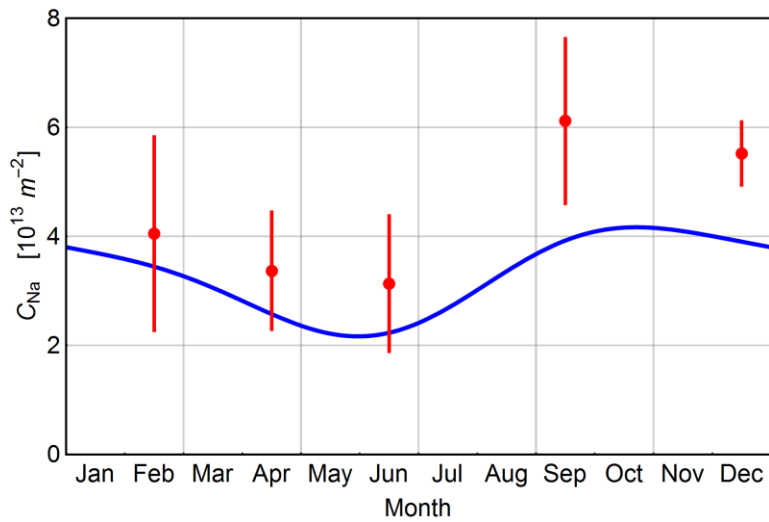


Figure 17. Median measured sodium abundance  $C_{Na}$  for each mission (red dots) with standard deviations (red bars) compared with a fit function to GOMOS global satellite data from Fussen *et al.* [11], evaluated at the Teide latitude 28.3°N

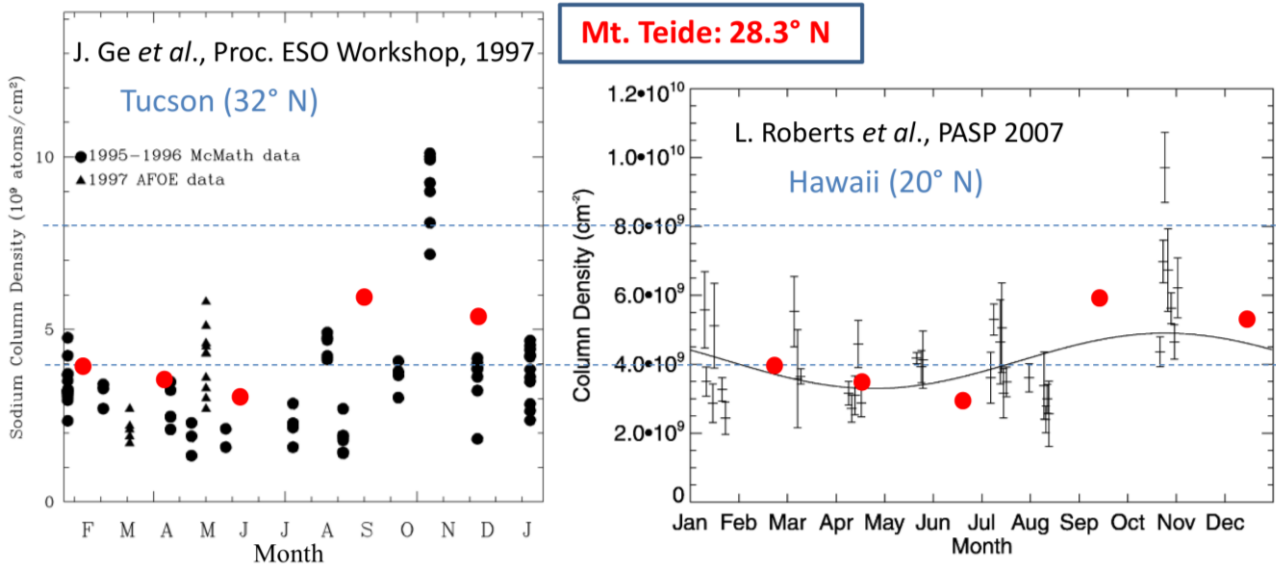


Figure 18. Median measured sodium abundance  $C_{Na}$  for each mission (red dots) drawn into annual plots from two literature references [12,13]. The dashed lines run at  $C_{Na} = 4 \times 10^{13}$  atoms/m<sup>2</sup> and  $8 \times 10^{13}$  atoms/m<sup>2</sup>.

### 3. CONCLUSIONS

We have used the data of an observing campaign with the ESO 20-watt transportable sodium LGS system *Wendelstein* at Observatorio del Teide on Tenerife (Canary Islands, 28.3°N), comprising five observing missions of about one week each, spread over 12 months. The specifications of this laser system and the employed Raman fiber laser technology are similar to those of the lasers in the 4LGSF/AOF [3] installed on the VLT on Cerro Paranal, Chile.

The LGS return flux was measured during these campaigns while varying the laser power, polarization, and D<sub>2b</sub> line repumping. In this work, we have compared the observations data with density matrix computer simulations using the package *LGSBloch* with custom extensions.

Overall, the agreement between observations and simulation is good, in some cases very good and in others poor. Of the five missions, the first two in June and September 2015 enjoyed the best seeing conditions and the agreement in these missions tends to be the best. Conversely, there are indications that the poor agreement cases may have suffered from adverse observing conditions.

We found a median sodium abundance of  $C_{\text{Na}} = 4.1 \times 10^{13}$  atoms/m<sup>2</sup> and the seasonal evolution of all five missions lies within the error bars found in literature references. Moreover, we derive the sodium coupling efficiency  $s_{\text{CE}}$  of *Wendelstein* with values in the range 187–300 photons/sr/s/W/(atoms/m<sup>2</sup>). For comparison, the 4LGSF/AOF specifies a flux of  $7.7 \times 10^6$  photons/s/m<sup>2</sup> when pointing at zenith assuming  $C_{\text{Na}} = 4 \times 10^{13}$  atoms/m<sup>2</sup>, corresponding to  $s_{\text{CE}} = 120$  photons/sr/s/W/(atoms/m<sup>2</sup>). The Thirty Meter Telescope (TMT) project specifies  $s_{\text{CE}} = 130$  photons/sr/s/W/(atoms/m<sup>2</sup>) for its LGS lasers [14].

In future publications, we intend to study the influence of laser linewidth, D<sub>2b</sub> repumping frequency offset, and the sensitivity of the fitted  $C_{\text{Na}}$  to seeing and vertical sodium density profiles.

### REFERENCES

- [1] Bonaccini Calia, D., Centrone, M., Lombardi, G. *et al.*, “LGS Return Flux: Report on the Tenerife optimization experiments and comparison with the Toptica laser results at the VLT,” Proc. SPIE **9909**, 30 (2016)
- [2] Bonaccini Calia, D., Guidolin, I., Friedenauer, A. *et al.*, “The ESO transportable LGS Unit for measurements of the LGS photon return and other experiments,” Proc. SPIE **8450**, 1R (2012)
- [3] Hackenberg, W., Bonaccini Calia, D., Buzzoni, B. *et al.*, “Assembly and test results of the AOF laser guide star units at ESO,” Proc. SPIE **9148**, 91483O (2014)
- [4] Pedreros Bustos, F., Holzlohner, R., Budker, D. *et al.*, “Sodium vapor cell laser guide star experiments for continuous wave model validation,” Proc. SPIE **9909**, 210 (2016)
- [5] Holzlohner, R., Rochester, S. M., Bonaccini Calia, D. *et al.*, “Optimization of cw sodium laser guide star efficiency,” Astron. & Astrophys. **510**, 20 (2010)
- [6] *AtomicDensityMatrix* and *LGSBloch* packages are online available at <http://rochesterscientific.com/ADM/>
- [7] Holzlohner, R., Rochester, S.M., Pfrommer, T. *et al.*, “Laser guide star return flux simulations based on observed sodium density profiles,” Proc. SPIE **7736**, 0V (2010)
- [8] Picone, J. M., Hedin, A. E., Drob, D. P. and Aikin, A. C., “NRLMSISE-00 empirical model of the atmosphere: Statistical comparisons and scientific issues,” J. Geophys. Res. **107** (A12), 1468 (2002)
- [9] Holzlohner, R., Bonaccini Calia, D. and Hackenberg, W., “Physical Optics Modeling and Optimization of Laser Guide Star Propagation,” Proc. SPIE **7015**, 701521 (2008)
- [10] Enderlein, M., Friedenauer, A., Schwerdt, R. *et al.*, “Series production of next-generation guide-star lasers at TOPTICA and MPBC,” Proc. SPIE **9148**, 914807 (2014)
- [11] Fussen, D., Vanhellefont, C., Tétard, N. *et al.*, “A global climatology of the mesospheric sodium layer from GOMOS data during the 2002–2008 period,” Atmos. Chem. Phys. Discuss. **10**, 6069–6127 (2010)
- [12] Ge, J., Angel, R., Jacobson, B. *et al.*, “Mesosphere Sodium Column Density and the Sodium Laser Guide Star Brightness,” Proc. ESO Workshop (1997)
- [13] Roberts, L. C. Jr., Bradford L. W., Newman C. R. and Liu, A. Z., “Measurements of Mesospheric Sodium Abundance above the Hawaiian Islands,” Proc. Astron. Soc. Pacific **119**, 787–792 (2007)
- [14] Boyer, C., Ellerbroek, B., and Gilles, L., “The TMT Laser Guide Star Facility,” Proc. AO4ELT 04004 (2010)